A Fast Sparse Azimuth Super-Resolution Imaging Method of Real Aperture Radar Based on Iterative Reweighted Least Squares With Linear Sketching

Xingyu Tuo, *Student Member, IEEE*, Yin Zhang, *Member, IEEE*, Yulin Huang, *Senior Member, IEEE*, and Jianyu Yang, *Member, IEEE*

***Abstract*—It is greatly significant to achieve radar forward-looking region imaging. Due to the limitation of phase ambiguity and small Doppler gradient in forward-looking region, synthetic aperture radar and Doppler beam sharpening cannot work for forward-looking imaging, while real aperture radar (RAR) has arbitrary imaging geometry. Nevertheless, restricted by the antenna aperture, azimuth resolution of RAR is coarse, super-resolution technology is required to improve its azimuth resolution. Exploiting the sparse prior information of the target, the super-resolution problem can be transformed into an L_1 norm minimization problem mathematically. Iterative reweighted algorithm can effectively solve the L_1 norm minimization problem by replacing L_1 norm with reweighted L_2 norm and computing the weight in each iteration. However, it suffers from a large computational load due to the repeated multiplications and inversions of large matrices. In this article, a fast azimuth super-resolution imaging method of RAR based on iterative reweighted least squares (IRLS) with linear sketching (LS) was proposed to achieve fast super-resolution imaging of RAR. The LS theory is employed to compress echo matrix and antenna measurement matrix into much smaller matrices via multiplying them by an embedded matrix. Then, the IRLS solver was utilized to address the reconstructed objective function. Much of the expensive computation can then be performed on the smaller matrices, thereby accelerating the algorithm. Simulations and experimental data prove that the proposed algorithm can offer a time complexity reduction without loss of imaging performance.**

***Index Terms*—Iterative reweighted least squares (IRLS), linear sketching (LS), real aperture radar (RAR), super-resolution imaging.**

I. Introduction

REAL aperture radar (RAR) has the advantage of an arbitrary imaging geometry and has been of considerable interest in applications where traditional synthetic aperture radar and Doppler beam sharpening are limited, such as airborne forward-looking ground mapping and aircraft forward-looking area navigation [1]–[4].

Manuscript received April 6, 2020; revised September 11, 2020; accepted February 9, 2021. Date of publication February 23, 2021; date of current version March 17, 2021. This work was supported in part by the National Natural Science Foundation of China under Grant 61901090 and Grant 61901092, and in part by the Collaborative Innovation Center of Information Sensing and Understanding. *(Corresponding author: Yin Zhang.)*

The authors are with the School of Information and Communication Engineering, University of Electronic Science and Technology of China, Chengdu 610054, China (e-mail: xingyu_tuo@163.com; yinzhang@uestc.edu.cn; yulinhuang@uestc.edu.cn; jyyang@uestc.edu.cn).

Digital Object Identifier 10.1109/JSTARS.2021.3061430

In order to obtain a high-resolution 2-D image, it is necessary to simultaneously improve range resolution and azimuth resolution. For the pulse signal, the range resolution is determined by the time-band product. To get high-range resolution, the linear frequency modulation (LFM) signal is transmitted to explore the information, which provides a large time-band product. Through impulse compression, the range resolution is improved to $\rho_r = c/2B$, in which B is signal bandwidth. Azimuth resolution is $\rho_a = R\lambda/D = R\theta$, where R is working distance, D is antenna aperture, θ is beamwidth. Seen from the formula, the azimuth resolution is constrained by the antenna aperture [5]–[7]. Theoretically, increasing physical aperture of the antenna can improve the azimuth resolution, but it is not feasible due to the limitation of platform resources. Consequently, the resolution in azimuth is usually much worse than a typical range resolution. For example, an RAR system whose carry frequency is 10 GHz, band width is 10 MHz, beamwidth is 4°, and working distance is 10 km. We can calculate that its range resolution ρ_r after pulse compression is 15 m, but its azimuth resolution ρ_a approximates 698 m. Therefore, in applications, the azimuth resolution needs to be improved first.

Under the Born hypothesis [8], the echo in the azimuth can be modeled as the convolution of target scattering coefficient and antenna pattern function. Therefore, the super-resolution methods based on deconvolution can improve the azimuth resolution in theory. However, due to the low-pass characteristics of the antenna pattern, antenna measurement matrix is ill-posed. Mathematically, super-resolution is equivalent to an ill-posed linear inversion problem.

Some super-resolution methods have been proposed. The method of truncated singular value decomposition (TSVD) has been put forward for radar imaging [9]–[11]. The author computed an approximation solution by chopping off those singular value components that are dominated by the noise. But the azimuth resolution increasement is slight due to truncation. In [12], a stable and effective approach based on Tikhonov regularization (REGU) was proposed. After investigated, the REGU and TSVD approach obtain similar resolution improvements. The iterative adaptive approach (IAA), which was presented in the application of passive array processing [13]–[15], was also applied to azimuth super-resolution [16]. However, since it requires the computation of the covariance matrix R, R^{-1}, and weighted least squares estimate for each sampled grid, the

improved performance of IAA comes at the cost of notably high computational complexity. In [17], a scheme of super-resolution based on maximum *a posteriori* framework is proposed. But this method finds solution iteratively, involving numerous matrix multiplication and inversion operations. To overcome the low-pass characteristics of the antenna in the frequency domain, spectrum extrapolation technology was proposed to recover the high-frequency components of the target and realize super-resolution imaging [18]–[21].

Recently, the sparse prior information of the target has been widely used to realize high-resolution imaging [22]–[26]. Research demonstrates that many targets of the imaging area possess the sparse scattering characteristic. Hence, based on the sparse characteristic, radar imaging processes can be deemed as a sparse reconstruction. For radar forward-looking imaging, applications such as aircraft forward-looking area navigation, weapon guidance, and target detection and recognition, require high resolution to enable quick detection of the target of interest [27]. The targets of interest are sparse compared with entire imaging region, especially for remote and large-scale imaging. Exploiting the sparse prior information of the target, the super-resolution problem both can be transformed into the L_1 norm minimization problem from the REGU framework or the Bayesian framework. Because the L_1 norm is not differentiable, solving L_1 REGU issue is a challenging task. At present, there are several methods to solve the L_1 norm minimization issue, such as alternating direction method of multipliers approach [28], [29], majorization–minimization (MM) algorithm [30], [31], iterative shrinkage threshold algorithm [32], split Bregman (SB) algorithm [33], [34], and iterative reweighted algorithm (IRA) [35].

Due to the nonsmooth nature of the L_1 norm, the abovementioned methods suffer a large computational complexity when solving the objective function. Therefore, in order to achieve fast solving, researchers have proposed various acceleration algorithms. The ideas of these acceleration algorithms are basically divided into the following two types: reducing the number of iterations and decreasing the computation complexity in a single iteration. The core of reducing the number of iterations is to accelerate convergence. For example, Zhang *et al.* [36] propose a fast majorization–minimization algorithm to improve computing efficiency. This method mainly uses the technique of vector extrapolation to predict the next iteration by the current and previous iterative information. By vector extrapolation, the required iterations for convergence are reduced. A fast iterative shrinkage-thresholding algorithm is employed in [37] and [38]. It is actually applying Nestrerov acceleration to the ISTA algorithm, increasing convergence rate from $O(1/k)$ to $O(1/k^2)$ to cut down iterations. Decreasing the computation complexity in a single iteration mainly comes from special matrix structure. In [39], by taking advantage of the Toplitz structure of the covariance matrix, the author exploits the Gohberg–Semencul representation to lower computational complexity of the inversion of the variance matrix. In [40], by exploiting the block tridiagonal structure of matrix, the author applies the divide and conquer strategy to accelerate the inversion.

As mentioned above, the IRAs, which contains iterative reweighted norm (IRN) and iterative reweighted least squares (IRLS), are a group of algorithms for effectively solving the L_1 norm minimization problem. The difference between IRLS and IRN is that the IRLS method introduces a constantly updated weight matrix based on the results of the least squares, and the IRN method introduces a constantly updated weight matrix based on the results of the L_2 norm. Least-squares solutions tend to be quite sensitive to data with large errors, thus, the IRLS method cannot be directly used to L_1 norm issue because of the ill-posed antenna measurement matrix in RAR super-resolution imaging. Only the IRN method can be directly used to solve the L_1 norm minimization problem in RAR super-resolution imaging. However, the IRN method need to update the weight matrix and target matrix at each iteration, involving complicated matrix multiplication and inversion operations. Therefore, in order to reduce computation complexity of single iteration, this article applies a strategy to reduce the size of matrices.

A fast sparse azimuth super-resolution imaging method of RAR is proposed in this article. The linear sketching (LS) technique is employed to project the high-dimensional antenna measurement matrix and echo matrix to low-dimensional space, which reduces the dimension of matrices. LS [41]–[44] technique comes from numerical linear algebra has attracted the attention of many researchers because the powerful concept of randomness has been introduced as a strategy to ease the computational load. This technology is widely used in robust regression problems, low rank approximation, and graph sparsification. The core of this technology is compressing a matrix to a much smaller one by multiplying it by a random embedded matrix. Much of the expensive matrix–matrix computation can then be performed on the smaller matrices, thereby accelerating the solution for the original problem. Then, based on processed result, L_1 sparse constraint is exploited to reconstruct objective function. Lastly, due to the ill-posedness of the antenna measurement matrix is alleviated after LS process, this article utilizes IRLS to solve the objective function. Compared with the IRN solver, the IRLS solver can obtain more obvious acceleration effects, as will be discussed later. Because of the reduction in the dimension of the matrices, computational complexity of matrix inversion and multiplications at single iteration decreases, effectively raising computational efficiency.

The remainder of this article is organized as follows. In Section II, the azimuth echo convolution model of RAR is derived. Section III has four the following sections: traditional IRN sparse super-resolution method and its computational complexity analysis is introduced; then comes antenna measurement matrix redundancy analysis; following is introduction of the LS technique; the proposed fast sparse azimuth super-resolution method and its computational complexity analysis is deduced at last. In Section IV, the effectiveness of the proposed method is verified by simulations and experimental data. Section V gives a brief conclusion.

II. Azimuth Echo Convolution Model

RAR uses a scanning mode to sweep the observation area and transmits chirps signal at a certain pulse repetition frequency (PRF). This article focuses on the mode of airborne RAR.

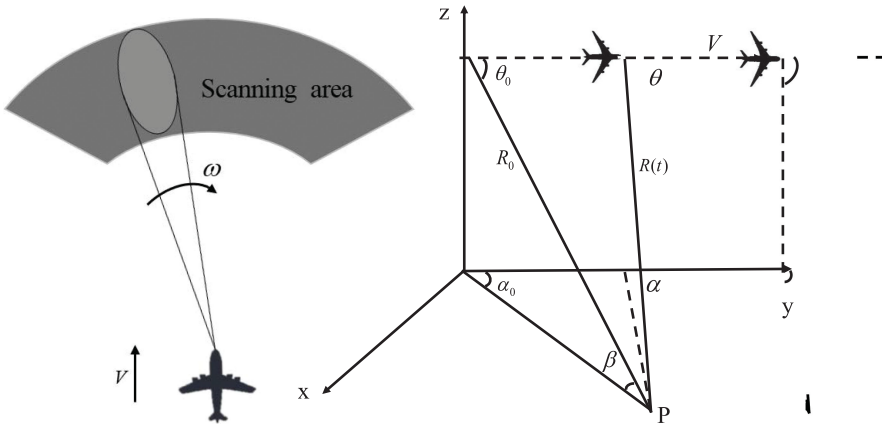

Fig. 1. (a) Imaging model of airborne RAR. (b) Geometry model of airborne RAR.

As illustrated in Fig. 1(a), an airborne RAR sweeps a narrow beam through the entire observation field that obtains 2-D microwave image. V is the platform movement speed and ω is the beam scanning speed. Fig. 1(b) illustrates the geometry model of airborne RAR, and target P is located at the forward-looking area (within the range of $\pm 10^\circ$ in the flight direction). The initial range between the radar and the target is denoted by R_0, and θ_0 denotes the initial spatial azimuth angle. The pitch angle is β, and grazing angle is α_0. When the aircraft flies with interval time t, the range history between the target and the aircraft becomes $R(t)$, the spatial azimuth angle changes into θ, and grazing angle turns into α.

According to the geometrical relationship, the range history $R(t)$ can be written as

$$R(t) = \sqrt{{R_0}^2 + V^2 t^2 - 2R_0 V t \cos\theta_0}. \tag{1}$$

The second-order Taylor expansion of (1) is

$$R(t) \approx R_0 - Vt\cos\theta_0 + \frac{V^2 \sin^2\theta_0}{2R_0} t^2. \tag{2}$$

In radar forward-looking imaging, the initial range R_0 is usually very large, and the spatial azimuth angle θ_0 is normally less than 10°, so the range history can be simplified as

$$R(t) \approx R_0 - Vt. \tag{3}$$

The transmitted LFM pulse can be expressed as follows:

$$y(\tau) = \text{rect}\left(\frac{\tau}{T_p}\right) \exp(j2\pi f_c \tau) \exp(j\pi k \tau^2) \tag{4}$$

where τ is fast time, representing range information. T_p is the pulsewidth of the transmitted signal. f_c is the carrier frequency, and k denotes frequency modulation ratio. rect$(.)$ is a rectangular window function: rect $= \begin{cases} 1, \tau \le |\frac{T_p}{2}| \\ 0, \text{other} \end{cases}$.

The echo after down-conversion can be denoted as follows:

$$y(\tau, t) = \sum x w(t) \text{rect}\left(\frac{\tau - \frac{2R(t)}{c}}{T_p}\right) \exp\left(j\pi k\left(\tau - \frac{2R(t)}{c}\right)^2\right) \exp\left(-j\frac{4\pi}{\lambda} R(t)\right) \tag{5}$$

where t is slow time, representing azimuth information. x represents the scattering coefficient of target. $w(t)$ is the modulation of the antenna pattern. $\frac{2R(t)}{c}$ is time delay. $\lambda = \frac{c}{f_c}$ is wavelength, $\exp[-j\frac{4\pi}{\lambda}R(t)]$ is the Doppler shift.

High-range resolution is achieved by pulse compression technique. Besides, due to movement of the platform, the range walk correction is required. According to (3), the echo signal can correct range walk by scale transformation. Echo after pulse compression and range walk correction becomes

$$y(\tau, t) = \sum x w(t) \sin c\left[B\left(\tau - \frac{2R_0}{c}\right)\right] \exp\left(-j\frac{4\pi}{\lambda} R(t)\right) \tag{6}$$

where B denotes the bandwidth.

The received signal can be transformed to range-angle domain, and the Doppler shift can usually be ignored due to small Doppler frequency gradient in the forward-looking area

$$\begin{aligned} y(R, \theta) &= \sum x(R, \theta) w(\theta - \theta_0) \sin c\left(\frac{2B}{c}(R - R_0)\right) \\ &= \sum x(R, \theta) \otimes \left[w(\theta) \sin c\left(\frac{2B}{c} R\right)\right]. \end{aligned} \tag{7}$$

The received echo can be considered as the convolution of the target scattering coefficient and the convolution kernel consisting of the antenna pattern in azimuth and the pulse modulation function in range direction. Since the range resolution has been advanced to $\frac{c}{2B}$ by pulse compression technology, only the azimuth echo is considered here. Next we only consider echo signal in one range bin. For a fixed range bin, (7) can be expressed as a 1-D convolution and rewritten in matrix form

$$\boldsymbol{y} = \boldsymbol{A}\boldsymbol{x} + \boldsymbol{n} \tag{8}$$

where $\boldsymbol{y} = [y_{(\theta_1)}, y_{(\theta_2)}, \ldots, y_{(\theta_n)}]^T$ is the received echo vector, $\boldsymbol{x} = [x_{(\theta_1)}, x_{(\theta_2)}, \ldots, x_{(\theta_n)}]^T$ is the vector of target scattering

coefficient, $\boldsymbol{n} = [n_{(\theta_1)}, n_{(\theta_2)}, \ldots, n_{(\theta_n)}]^T$ is the noise vector which satisfies Gaussian distribution. n represents the number of azimuth sampling points. $\boldsymbol{A}$ denotes the convolution matrix and can be written as follows:

$$\boldsymbol{A} = \begin{bmatrix} h_{(\theta_0)} & \cdots & h_{(\theta_{-l})} & & \\ \vdots & \ddots & & \ddots & \\ h_{(\theta_l)} & & \ddots & & h_{(\theta_{-l})} \\ & \ddots & & \ddots & \vdots \\ & & h_{(\theta_l)} & \cdots & h_{(\theta_0)} \end{bmatrix}_{n\times n}$$

where $[h_{(\theta_{-l})} \cdots h_{(\theta_0)} \cdots h_{(\theta_l)}]$ are the samples of the antenna pattern, the sampling number is determined by PRF, beamwidth, and antenna scanning velocity ω.

III. Proposed Method

In this section, we research the traditional IRN sparse super-resolution method and give its computational complexity first; second, we explore the redundancy of the antenna measurement matrix; third, we introduce LS theory; finally, the proposed IRLS–LS fast sparse super-resolution method and its computational complexity is deduced.

A. IRN Sparse Super-Resolution Method

Recovering the target scattering coefficient $\boldsymbol{x}$ from the noise-polluted echo data $\boldsymbol{y}$ is usually an ill-posed problem, thus, the REGU method is used to relax ill-posedness. The REGU method replaces the original ill-posed problem with a problem that is close to well-conditioned by adding different REGU constraints. The standard REGU function is as follows:

$$\hat{\boldsymbol{x}} = \arg\min_{\boldsymbol{x}} \frac{1}{p} \|\boldsymbol{y} - \boldsymbol{A}\boldsymbol{x}\|_p^p + \lambda \frac{1}{q} \|\boldsymbol{x}\|_q^q \tag{9}$$

where the value of p, q depends on the norm type you choose. $\frac{1}{p}\|\boldsymbol{y} - \boldsymbol{A}\boldsymbol{x}\|_p^p$ is the data fitting term, $\frac{1}{q}\|\Gamma(\boldsymbol{x})\|_q^q$ is is the added penalty term, λ is the positive parameter controlling the REGU strength.

For sparse super-resolution problem, usually the L_q norm with $0 \le q \le 1$ is employed as penalty function. We know that the stronger sparsity needs a smaller q. Finding the globally optimal solution is NP hard problem when $0 \le q < 1$. Therefore, researchers often use the L_1 norm to describe the sparse characteristics of the target. When $p = 2$, $q = 1$, the objection function is constructed as the following:

$$\hat{\boldsymbol{x}} = \arg\min_{\boldsymbol{x}} \|\boldsymbol{y} - \boldsymbol{A}\boldsymbol{x}\|_2^2 + \lambda\|\boldsymbol{x}\|_1. \tag{10}$$

As mentioned above, in the IRAs, only the IRN method can be directly used to solve the L_1 norm minimization problem in radar super-resolution imaging. We define the weight matrix $\boldsymbol{W} = \mathrm{diag}(|\boldsymbol{x}|^{-1})$. Weight matrix $\boldsymbol{W}$ will be updated by the scattering coefficients $\boldsymbol{x}$. Hence, the optimal solution is obtained by the iteration process. The initial value of $\boldsymbol{x}_0$ should be given by Tikhonov REGU. The iterative process is described as follows:

$$\text{initialize}: \boldsymbol{x}_0 = (\boldsymbol{A}^T\boldsymbol{A} + \lambda\boldsymbol{I})^{-1}\boldsymbol{A}^T\boldsymbol{y}$$

$$\text{for } j = 0, 1, 2, \ldots, M-1$$

$$\boldsymbol{W}_j = \mathrm{diag}(|\boldsymbol{x}_j|^{-1})$$

$$\boldsymbol{x}_{j+1} = (\boldsymbol{A}^T\boldsymbol{A} + \lambda\boldsymbol{W}_j)^{-1}\boldsymbol{A}^T\boldsymbol{y} \tag{11}$$

In the IRN method, the dimension of $\boldsymbol{A}$ is $n \times n$, and the dimension of $\boldsymbol{y}$ is $n \times 1$. Table I shows the computational complexity of the IRN method, where M is the number of iterations.

B. Antenna Measurement Matrix Analysis

From the abovementioned analysis, we can see that the traditional IRN sparse super-resolution method has numerou $n \times n$ matrix multiplication and inversion operations, which is the main reason for slow running speed. In this section, we analyze the redundancy of the antenna measurement matrix to lay foundation for the subsequent LS.

Matrix decomposition theory is adopted to analyze the information redundancy. The singular value decomposition (SVD) operation is applied to antenna measurement matrix $\boldsymbol{A}$

$$\boldsymbol{A} = \boldsymbol{U}\boldsymbol{\Sigma}\boldsymbol{V} = \sum_{i=1}^{n} u_i \sigma_i {v_i}^T \tag{12}$$

where $\boldsymbol{U} = (u_1, u_2, \ldots, u_n)$ and $\boldsymbol{V} = (v_1, v_2, \ldots, v_n)$ are the unitary matrices with size $n \times n$, respectively. $\boldsymbol{\Sigma} = \begin{pmatrix} \boldsymbol{D} & 0 \\ 0 & 0 \end{pmatrix}$, $\boldsymbol{D} = \mathrm{diag}(\sigma_1, \sigma_2 \cdots, \sigma_n)$, σ_{i} is the singular value of $\boldsymbol{A}$ and satisfies $\sigma_1 > \sigma_2 > \sigma_i > \cdots > \sigma_n$.

The following figure is the singular value distribution of $\boldsymbol{A}$ with different size. From the perspective of matrix redundancy, the SVD theory holds that the information of the matrix is only contained in the large singular values and their corresponding eigenvectors and small singular values and their eigenvectors contain almost no information. From Fig. 2, the antenna measurement matrix $\boldsymbol{A}$ has most singular values close to zero whatever the size it is, which shows the redundant property of antenna measurement matrix $\boldsymbol{A}$. The small singular values bring the increasement of the computational complexity and are the root cause of redundancy. From the perspective of matrix ill-posedness, the condition number of a matrix measures the ill-posed nature of this matrix. When the condition number is large, the estimation error will be big when noise exists. The condition number is the ratio of the largest singular value to the smallest singular value of the matrix. As can be seen from Fig. 2, the condition number of the antenna measurement matrix, $\mathrm{cond}(\boldsymbol{H}) = \frac{\sigma_1}{\sigma_n}$, is considerably large whatever the size it is, which shows the ill-posed property of it. Hence, the small singular values are root cause of matrix ill-posedness.

For example, when the antenna measurement matrix $\boldsymbol{A}$ is 667×667, and only 17 dominant singular values are > 1, and other 650 small singular values are information redundant. If the information contained in 17 large singular values and their corresponding eigenvectors can be used to represent the original antenna measurement matrix, it will reduce its redundancy and ill-posedness.

TABLE I
COMPUTATIONAL COMPLEXITY OF THE IRN

update x_0	update W	update x_j	total computational complexity
$O(3n^3+n^2+n)$	negligible	$O(M(3n^3+n^2+n))$	$O((3M+3)n^3+(M+1)n^2+(M+1)n)$

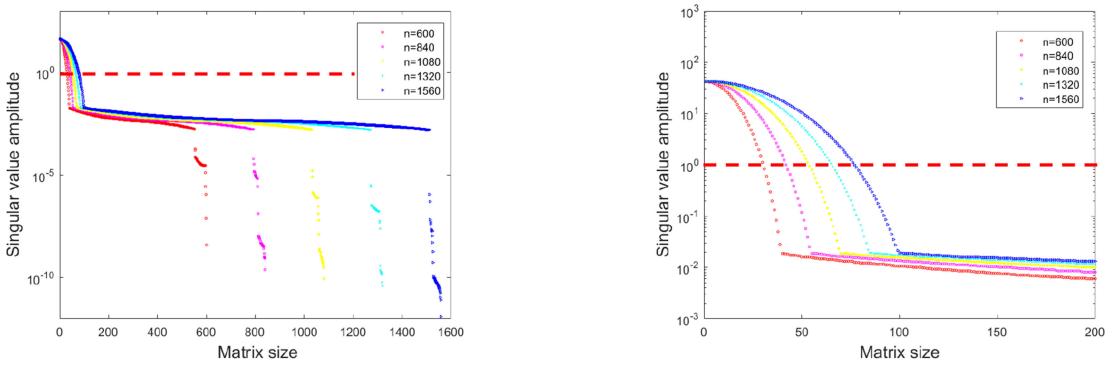

Fig. 2. Singular value distribution of $\boldsymbol{A}$ with different size. (a) All singular values distribution. (b) First 200 singular values distribution.

C. Linear Sketching

Due to the redundant property of the antenna measurement matrix $\boldsymbol{A}$, this article utilizes the LS method to modify the redundant property.

The task of LS is to construct a near-optimal basis $\boldsymbol{Q}$ that captures the action of the matrix $\boldsymbol{A}$. In other words, we require a matrix $\boldsymbol{Q}$ for which $\boldsymbol{Q}$ $(n \times q)$ has orthonormal columns and the number of columns is $q(q \ll n)$

$$\boldsymbol{A} \approx \boldsymbol{Q}(\boldsymbol{Q}^T\boldsymbol{A}). \tag{13}$$

For convenience, the matrix $\boldsymbol{Q}^T(q \times n)$ is called as the embedded matrix, which converts the space described by $\boldsymbol{A}$ into a low-dimension space; and the smaller matrix $\boldsymbol{Q}^T\boldsymbol{A}$ is named as the information carrying matrix, which contains the main information of $\boldsymbol{A}$ and can then be used to compute original problem.

In order to improve the calculation efficiency, it would like matrix $\boldsymbol{Q}$ to contain as few columns as possible, but it is even more important to have an accurate approximation of the input matrix. There is a tradeoff between the calculation efficiency and approximation error, so how to choose the number of columns q is the core problem.

Suppose we are given a matrix $\boldsymbol{A}$ and a positive error tolerance ε. We seek a matrix $\boldsymbol{Q}$ with $q = q(\varepsilon)$ orthonormal columns such that

$$\left\|\boldsymbol{A}-\boldsymbol{Q}(\boldsymbol{Q}^T\boldsymbol{A})\right\| \le \varepsilon \tag{14}$$

where $\|\cdot\|$ denotes the L_2 operator norm. The $\boldsymbol{Q}^T$ is a $q \times n$ dimensional subspace that captures most of the action of $\boldsymbol{A}$. Obviously, the larger columns q indicates the smaller error ε.

The SVD furnishes an optimal answer to this problem [45], [46]. Let σ_j denotes the j_{th} largest singular value of $\boldsymbol{A}$. For each $j \ge 0$

$$\min_{\mathrm{k}\le j}\left\|\boldsymbol{A}-\boldsymbol{Q}\boldsymbol{Q}^T\boldsymbol{A}\right\| = \sigma_{j+1}. \tag{15}$$

That is, for each $j \ge 0$, when the columns $q = j$, the approximation error is σ_{j+1}. According to the SVD theory, the main information of the matrix is contained in the large singular values and their corresponding eigenvalue vectors, small singular values and their eigenvectors contain almost no information. So we can choose the number of dominant singular values needed as the value of columns q. Hence, this article offers a reasonable method of selecting parameter q. The columns q can be equivalent to the truncation parameter k in the TSVD method. The generalized cross-validation (GCV) is described in [47], which has been proven to be an excellent method of choosing a truncation parameter. The optimal truncation parameter k can be obtained by minimizing the GCV function

$$k = \arg\min_k \frac{\|\boldsymbol{A}\boldsymbol{x}_k-\boldsymbol{y}\|_2^2}{\mathrm{trace}(\boldsymbol{I}-\boldsymbol{A}\boldsymbol{A}_k^+)} \tag{16}$$

where $\boldsymbol{A}_k^+$ satisfies $\boldsymbol{A}_k^+\boldsymbol{y} = \boldsymbol{x}_k$. $\boldsymbol{I}$ represents the identity matrix. trace$(\cdot)$ denotes the sum of the diagonal components inside the brackets.

The optimal truncation parameter k is determined by the environment and system parameters, and can be deduced offline in advance. Therefore, this article assumes that k is known in advance.

The next task is to build the matrix $\boldsymbol{Q}$. In order to ensure the performance and stability, we require the matrix $\boldsymbol{Q}$ to be random and has orthogonal columns [48], [49]. There are several ways to construct the matrix $\boldsymbol{Q}$, such as selecting the q dominant left singular vectors of $\boldsymbol{A}$. $\boldsymbol{Q}$ also can be a Subsampled Randomized Hadamard Transform, which is formulated as $\boldsymbol{Q} = \mathbf{P} \times \mathbf{S} \times \mathbf{D}$. The $\mathbf{D}$ is a diagonal matrix with +1,−1 on diagonals. $\mathbf{S}$ is the Hadamard transform. The $\mathbf{P}$ is just chooses a random (small)

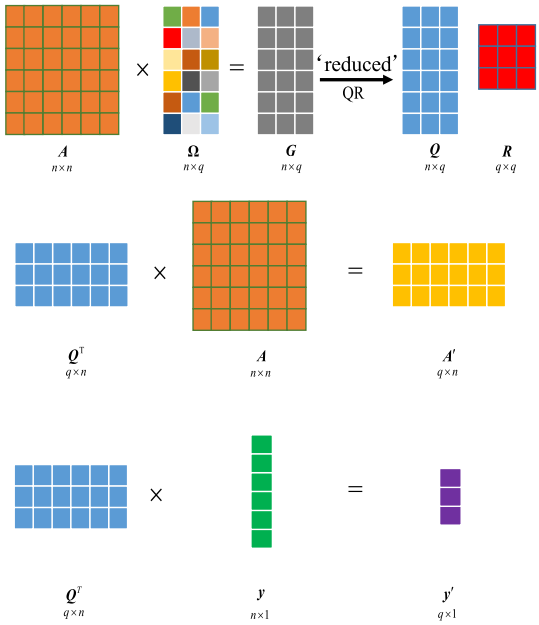

Fig. 3. Conceptual architecture of LS preprocessing. First, a matrix $\boldsymbol{Q}$ is computed in order to derive the embedded matrix $\boldsymbol{Q}^T$. Then, the embedded matrix $\boldsymbol{Q}^T$ is utilized to deduce the smaller matrix $\boldsymbol{A}'$ and $\boldsymbol{y}'$.

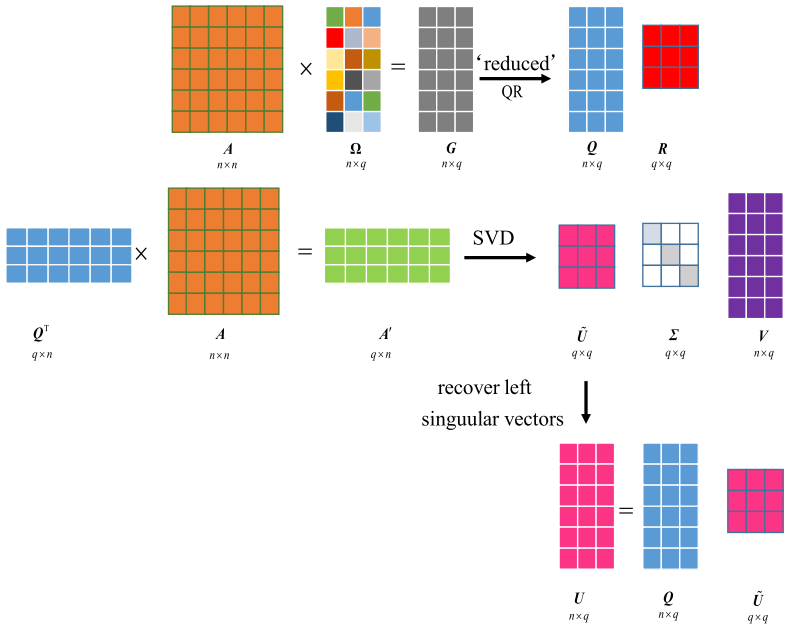

Fig. 4. Conceptual architecture of the randomized singular value decomposition (RSVD).

subset of rows of $\mathbf{S} \times \mathbf{D}$. This article introduces a method based on QR decomposition to obtain $\boldsymbol{Q}$ with orthogonal columns.

1) Generate a $n \times q$ Gaussian random matrix $\boldsymbol{\Omega}$ with a mean of 0 and a variance of 1.

2) Form the matrix $\boldsymbol{G} = \boldsymbol{A\Omega}$.

3) Obtain the matrix $n \times q$ $\boldsymbol{Q}$ via QR decomposition of $\boldsymbol{G}$.

This article transposes the generated matrix $\boldsymbol{Q}$ to acquire the embedded matrix $\boldsymbol{Q}^T$, which projects antenna measurement matrix $\boldsymbol{A}$ and echo matrix $\boldsymbol{y}$ to a low-dimensional space. Thus, (8) is converted into

$$\boldsymbol{Q}^T\boldsymbol{y} = \boldsymbol{Q}^T\boldsymbol{A}\boldsymbol{x} + \boldsymbol{Q}^T\boldsymbol{n}. \tag{17}$$

For convenience, let $\boldsymbol{y}' = \boldsymbol{Q}^T\boldsymbol{y}$, $\boldsymbol{A}' = \boldsymbol{Q}^T\boldsymbol{A}$, $\boldsymbol{n}' = \boldsymbol{Q}^T\boldsymbol{n}$. The convolution model of (8) is reconstructed as following.

$$\boldsymbol{y}' = \boldsymbol{A}'\boldsymbol{x} + \boldsymbol{n}' \tag{18}$$

where $\boldsymbol{y}'$ is a $q \times 1$ reconstructional echo matrix, $\boldsymbol{A}'$ is a $q \times n$ reconstructional antenna measurement matrix, and $\boldsymbol{n}'$ is a $q \times 1$ reconstructional noise matrix. To intuitively illustrate whole LS process: including how to construct the basis matrix $\boldsymbol{Q}$, and use $\boldsymbol{Q}$ to compress the matrix $\boldsymbol{A}$ and $\boldsymbol{y}$, this article offers a diagram in Fig. 3.

D. Proposed IRLS–LS Fast Sparse Super-Resolution Method

After LS process, the convolution model is reconstructed as (18). L_1 norm is employed as an REGU term to establish objective function under REGU framework

$$\hat{\boldsymbol{x}} = \arg\min_{\boldsymbol{x}} \|\boldsymbol{A}'\boldsymbol{x} - \boldsymbol{y}'\|_2^2 + \lambda\|\boldsymbol{x}\|_1. \tag{19}$$

Since the antenna measurement matrix $\boldsymbol{A}$ and echo matrix $\boldsymbol{y}$ become smaller matrices $\boldsymbol{A}'$ and $\boldsymbol{y}'$ after LS. If the IRN method is still applied to minimize the objective function, we can easily observe that the dimensions of matrix–matrix multiplication are reduced. However, the dimension of $(\boldsymbol{A}'^T\boldsymbol{A}' + \lambda\boldsymbol{W}_j)^{-1}$ in each iteration is still $n \times n$, acceleration effect is not powerful. Thus, the IRLS method is applied to minimize the objective function.

As mentioned above, the IRLS method cannot be used directly to solve L_1 norm in RAR super-resolution imaging unless ill-posedness of antenna measurement matrix is relaxed. In the following, we analyze its ill-posedness. According to randomized singular value decomposition (RSVD) theory [50], [51], we have

$$\begin{aligned}\boldsymbol{A} &\approx \boldsymbol{Q}(\boldsymbol{Q}^T\boldsymbol{A}) = \boldsymbol{Q}\boldsymbol{A}' = \boldsymbol{Q}\tilde{\boldsymbol{U}}\boldsymbol{\Sigma}\boldsymbol{V}^T \\ &= \boldsymbol{U}_{n\times q}\boldsymbol{\Sigma}_{q\times q}{\boldsymbol{V}_{n\times q}}^T = \boldsymbol{A}_q.\end{aligned} \tag{20}$$

The conceptual architecture of the RSVD is visually illustrated in Fig. 4. We can see that the RSVD uses the same way to obtain matrix $\boldsymbol{A}'$ as the LS process shown in Fig. 3. Fig. 4 clearly indicates that $\boldsymbol{A}'$ only contains q dominant singular values and corresponding right singular value vectors. The condition number of $\boldsymbol{A}'$ is $\text{cond}(\boldsymbol{A}') = \frac{\sigma_1}{\sigma_q}$, which is considerably lower than $\text{cond}(\boldsymbol{A}) = \frac{\sigma_1}{\sigma_n}$. Through LS process, a decrease in condition number indicates that the ill-posedness is relaxed, hence, the IRLS method can be applied to solve L_1 minimization problem in (19).

The IRLS approach is to replace the L_1 objective function in (19) by solving the following weighted L_2 norm problem:

$$\min \sum_{i=1}^{n} w_i({x_i}^{(j)})^2, \text{ subject to } \boldsymbol{A}'\boldsymbol{x} = \boldsymbol{y}' \tag{21}$$

where the weights w_i are computed from the previous iterate $\boldsymbol{x}^{(j-1)}$, j is number of iterations. ${x_i}^{(j)}$ is the i_{th} entry of target

TABLE II
FLOW CHART OF THE IRLS–LS FAST SPARSE SUPER-RESOLUTION METHOD

Generate a $n \times q$ Gaussian random matrix $\boldsymbol{\Omega}$
Form the matrix $\boldsymbol{G}=\boldsymbol{A\Omega}$
Obtain the matrix $\boldsymbol{Q}$ via $\boldsymbol{G}=\boldsymbol{QR}$
$\boldsymbol{y'} = \boldsymbol{Q}^T\boldsymbol{y}$, $\boldsymbol{A'} = \boldsymbol{Q}^T\boldsymbol{A}$
initialization: $\boldsymbol{x}^{(0)} = \boldsymbol{A'}^T(\boldsymbol{A'}\boldsymbol{A'}^T)^{-1}\boldsymbol{y'}$, $\varepsilon = 1 \times 10^{-6}$
While $j = 1 : M, do$
$\boldsymbol{W}^{(j)} = diag(((x_i^{(j-1)})^2+\varepsilon)^{-\frac{1}{2}})$
$\boldsymbol{x}^{(j)} = \boldsymbol{W}^{(j)}\boldsymbol{A'}^T(\boldsymbol{A'}\boldsymbol{W}^{(j)}\boldsymbol{A'}^T)^{-1}\boldsymbol{y'}$
$j = j + 1$
end

scattering coefficient matrix $\boldsymbol{x}$ at j_{th} iteration. So that the objective in (21) is a first-order approximation to the L_1 objective function. The solution of (21) can be offered explicitly, giving the next iterate $\boldsymbol{x}^{(j)}$:

$$\boldsymbol{x}^{(j)} = \boldsymbol{W}^{(j)}\boldsymbol{A}'^T(\boldsymbol{A}'\boldsymbol{W}^{(j)}\boldsymbol{A}'^T)^{-1}\boldsymbol{y}' \tag{22}$$

where $\boldsymbol{W}^{(j)}$ is the diagonal matrix with entries $1/w_i = |x_i{}^{(j-1)}|$. However, the weights w_i are undefined whenever $x_i^{(j-1)} = 0$. A common approach for dealing with this issue is to regularize the optimization problem, by incorporating a small $\varepsilon > 0$

$$w_i = ((x_i^{(j-1)})^2 + \varepsilon)^{-\frac{1}{2}}. \tag{23}$$

Initialization $\boldsymbol{x}^{(0)}$ is given by least squares result in the IRLS approach. Hence, the detailed process is shown as follows. To explain the complete process of the proposed IRLS–LS fast sparse super-resolution method perspicuously, this article lists it in Table II

$$\begin{aligned} \text{Intialize}: \boldsymbol{x}^{(0)} &= \boldsymbol{A'}^T(\boldsymbol{A'}\boldsymbol{A'}^T)^{-1}\boldsymbol{y'} \\ \text{for} \quad j &= 1, 2, 3 \ldots, M \\ \boldsymbol{W}^{(j)} &= \text{diag}(((x_i^{(j-1)})^2+\varepsilon)^{-\frac{1}{2}}) \\ \boldsymbol{x}^{(j)} &= \boldsymbol{W}^{(j)}\boldsymbol{A'}^T(\boldsymbol{A'}\boldsymbol{W}^{(j)}\boldsymbol{A'}^T)^{-1}\boldsymbol{y'} \\ &\text{end} \end{aligned} \tag{24}$$

The computational complexity analysis of the proposed algorithm is conducted. We compute the matrix products $\boldsymbol{G} = \boldsymbol{H\Omega}$ to take a running time in $O(nnz(\boldsymbol{H})q)$, where $nnz(\boldsymbol{H})$ is the number of nonzeros in $\boldsymbol{H}$. A QR-factorization in time $O(nq^2)$ gives $\boldsymbol{Q}$. Computing $\boldsymbol{y'} = \boldsymbol{Q}^T\boldsymbol{y}$, $\boldsymbol{A'} = \boldsymbol{Q}^T\boldsymbol{A}$ takes $O(n^2q + nq)$ time. Hence, the computational complexity of LS process is $O(n^2q + (q^2 + q)n + nnz(\boldsymbol{A})q)$. In the IRLS–LS method, the dimension of $\boldsymbol{A'}$ is $q \times n$, and the dimension of $\boldsymbol{y'}$ is $q \times 1$. Table III shows the computational complexity of the IRLS–LS method, where M is the number of iterations. Compared with the IRN method shown in Table I, the price paid by the proposed method is the extra computational load coming from the LS process. Although LS process brings additional computational burden, it can reduce the size of the matrices. In addition, due to the IRLS solver, the computational complexity is significantly reduced when calculating $\boldsymbol{x}^{(0)}$ and $\boldsymbol{x}^{(j)}$. Hence, the proposed method is better than the IRN method in terms of computational efficiency, especially when the number of azimuth sampling points n is large, the advantages of our proposed algorithm are more obvious.

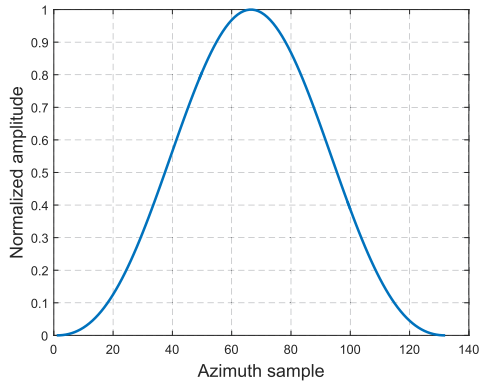

Fig. 5. Antenna pattern for simulations.

IV. SIMULATIONS AND EXPERIMENTAL DATA RESULTS

In this section, some simulations and experiments are conducted to prove the superior imaging performance and computation efficiency of the proposed fast l_1-IRLSLS algorithm. Simulation and experiment result are compared with conventional super-resolution imaging methods, including the TSVD method, IAA, and the l_1 sparse REGU method solved by IRN, which is called the l_1-IRN method for convenience next. This article mainly focuses on the super-resolution performance and operation time of the various algorithms. For the TSVD approach, the number of reserved singular value is determined by the GCV [47]. The REGU parameter of the l_1-IRN method is selected by the L-curve method [52]. In addition, for different sparse methods, this article also gives a comparison of computation time curve.

A. 1-D Point Target Simulation

First, this article conducts point simulation. The antenna pattern for simulations is a $\sin c^2$ function illustrated is Fig. 5, whose main beamwidth is 3.5°. The scanning region is ±10°. The 1-D simulation scene is illustrated in Fig. 7(a), we can see that there are two point targets whose width are 1° with identical amplitude, and their centers are located at 0° and 2°, respectively. The simulation system parameters are shown in Table IV. Simulation hardware and software environment is shown in Table V. In order to simulate the actual working environment, Gaussian white noise is added. Here, we define the signal to noise ratio (SNR) as follows:

$$\text{SNR} = 10\log 10\frac{\|\boldsymbol{x}\|_2^2}{\|\boldsymbol{y} - \boldsymbol{Ax}\|_2^2}. \tag{25}$$

In order to quantify and compare the imaging performance, the difference of peak to valley (DPV) in dB and peak signal to noise ratio (PSNR) is used in this section. The DPV point in

TABLE III
COMPUTATIONAL COMPLEXITY OF THE IRLS–LS

linear sketching	update $\boldsymbol{x}^{(0)}$	update $\boldsymbol{W}$	update $\boldsymbol{x}^{(j)}$	total computational complexity
$O(n^2q+(q^2+q)n+nnz(\boldsymbol{A})q)$	$O(2n^2q+nq+q^3)$	negligible	$O(M(2n^2q+3nq+q^3))$	$O((2Mq+3q)n^2+(3Mq+q^2+2q)n+(M+1)q^3+nnz(\boldsymbol{A})q)$

TABLE IV
SIMULATION SYSTEM PARAMETERS

Parameter	Value
Carrier frequency	35 GHz
Bandwidth	80 MHz
Pulse interval	$2\times10^{-6}s$
Antenna scanning velocity	$60\ ^\circ/s$
Main beam width	$3.5\ ^\circ$
Plus repetition frequency	1000 Hz

TABLE V
SIMULATION CONDITIONS

Hardware or Software	Parameters
CPU	Inter(R) Core(TM)i5-4200M CPU
RAM	8 GB
Platform	MATLAB 2015b

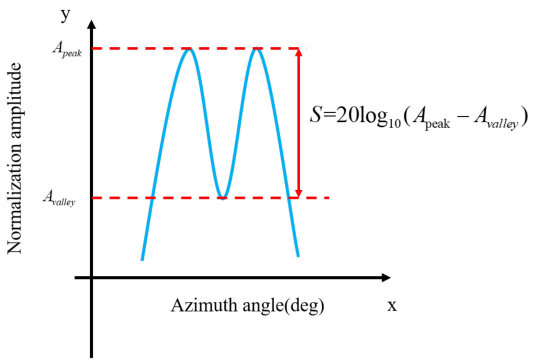

Fig. 6. Definition of DPV.

dB is interpreted in Fig. 6, and quantifies the ability of super-resolution algorithm to separate two closely spaced targets. The DPV in dB is between 0 and $-\infty$, where 0 means the angular super-resolution method can fully separate two closely spaced targets. This indicates that the larger value of peak to valley in dB, the better performance of the proposed super-resolution method in terms of the super-resolution performance. PSNR is used to measure the side lobe suppression. The PSNR is defined as

$$\mathrm{PSNR}=20\log_{10}\frac{s_{\max}}{sl_{\max}} \tag{26}$$

where $s_{\max}$ and $sl_{\max}$ denote the maximum amplitude of signal and side lobe. When PSNR value is large, it indicates that the corresponding super-resolution algorithm has strong side lobe suppression capability.

TABLE VI
ALGORITHM PARAMETERS AND CT OF 1-D SIMULATION

Algorithm	Parameters	CT
TSVD	$k=17$	0.204542 s
IAA	$\lambda=10,\ a=100$	0.215984 s
l_1-IRN	$\lambda=10,\ \mu=2$	0.204542 s
fast l_1-IRLSLS	$\lambda=10,\ q=17$	0.090796 s

TABLE VII
SUPER-RESOLUTION PERFORMANCE COMPARISON OF 1-D SIMULATION

Algorithm	DPV in dB	PSNR
TSVD	-6.9570 dB	10.0642 dB
IAA	-1.8078 dB	37.0774 dB
l_1-IRN	-0.9577 dB	37.0095 dB
fast l_1-IRLSLS	-0.4455 dB	31.7005 dB

For each algorithm, the relative parameter values and computing time (CT) are shown in Table VI. k denotes the truncation parameter of the TSVD method, a denotes the weighting parameter in the IAA method, μ is REGU parameter of the l_1-IRN method, q denotes the subspace dimension. λ is the number of iterations of IAA, the l_1-IRN method and the proposed fast l_1-IRLSLS method. Note that the meaning of these symbols runs through all experiments. Table VII is the super-resolution performance comparison of various algorithms, which contains DPV in dB and PSNR.

Fig. 7 shows point simulation results. Fig. 7(a) is the 1-D simulation scene. Fig. 7(b) is the real-beam echo polluted by Gaussian noise. From the scanning region, PRF, and scanning velocity, we can calculate echo size to be 334×1. Due to the interval of two point targets is less than the beam width, the echoes of two targets are overlapped. Fig. 7(c) is the result processed by the TSVD method. The two targets can be distinguished to a certain degree, but the sidelobes are raised. Fig. 7(d) is the result of the IAA method. Compared with the TSVD method, it has higher resolution and lower side lobes. Fig. 7(e) and (f) is the result of the l_1-IRN method and the fast l_1-IRLSLS method, respectively. They have the superior super-resolution performance than TSVD and IAA method visibly. From Table VII, we can clearly see that the DPV in dB of these two methods are far higher than other methods. However, as shown in Table VI, the l_1-IRN method and the IAA method need to take more time than our proposed fast l_1-IRLSLS method.

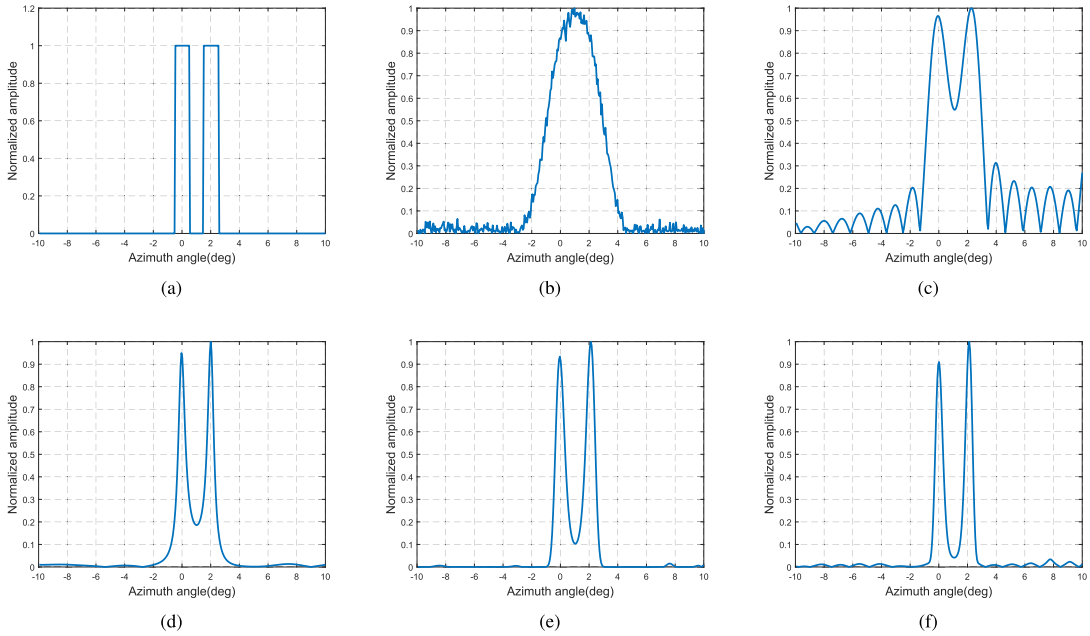

Fig. 7. 1-D point simulation result. (a) 1-D simulation scene. (b) Echo in SNR = 25 dB. (c) TSVD method. (d) IAA method. (e) l_1-IRN method. (f) Proposed fast l_1-IRLSLS method.

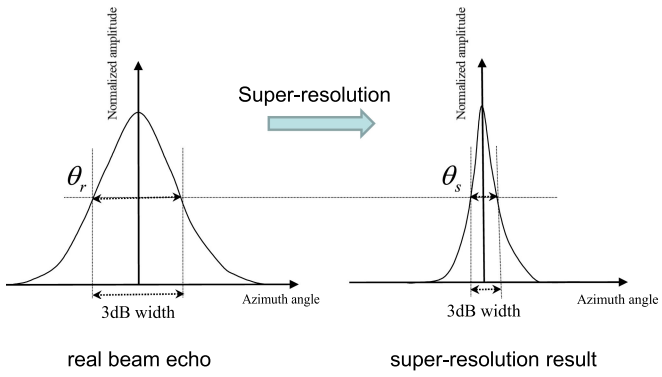

Fig. 8. Definition of BSR.

B. 2-D Area Simulation

In the last section, this article has proven that our proposed method can achieve super-resolution imaging of 1-D point targets, and in this section, we will discuss area simulation. The antenna pattern, and simulation hardware and software environment are the same with 1-D simulation. The scanning region is $\pm 5^\circ$. The area simulation scene is illustrated in Fig. 9(a). The original scene consisted of three groups of adjacent targets at distances of 9085, 9160, and 9225 m, as well as one island target at a distance of 9300 m. The size of the simulation scene is 200×200, and the size of each target is 11×8, which means the azimuth width of each target is 0.55°. The azimuth interval between adjacent targets at 9085 m is 4.05°, the azimuth interval between targets at 9160 m is 2.65°, and the azimuth interval between targets at 9225 m is 1.60°.

In addition, some quantitative indexes are exploited to measure the super-resolution performance. For the area scene, the mean square error (MSE) is utilized to evaluate the closeness between the original scene and super-resolution result. The ideal MSE is 0, which means the super-resolution result and the original scene are the same. A smaller value of the MSE indicates a better performance of the approach in terms of imaging quality

$$\mathrm{MSE} = \frac{1}{MN} \|\boldsymbol{\sigma} - \hat{\boldsymbol{\sigma}}\|_2^2 \tag{27}$$

where M and N are the numbers of discretization bins of range and azimuth, respectively. $\boldsymbol{\sigma}$ is the original scene, and $\hat{\boldsymbol{\sigma}}$ is super-resolution result.

Beam sharpening ratio (BSR) is defined as follows: the ratio that the original real beam 3 dB bandwidth divides super-resolution processing result 3 dB bandwidth, shown in Fig. 8

$$\mathrm{BSR} = \frac{\theta_r}{\theta_s}. \tag{28}$$

BSR measures the ability of super-resolution, the larger BSR indicates higher resolution.

Similarly, CT and algorithm parameters are shown in Table VIII. And comparison of quantitative indexes results is in Table IX. The area simulation results are shown in Fig. 9. Fig. 9(a) is the simulation scene. Fig. 9(b) is the real beam echo result. Echo size of the area simulation is 598×167, but we resize it to 200×200 when displaying the results. Fig. 9(b) suffers from coarse azimuth resolution, and it can be seen that all the adjacent targets could not be distinguished. Fig. 9(c) is the result of the TSVD method. Although it improves the resolution to a certain degree, it brings a lot of ghosts, which seriously affects the image quality. Fig. 9(d) is the result of the IAA method. It has a good super-resolution performance, but some targets are blurry and

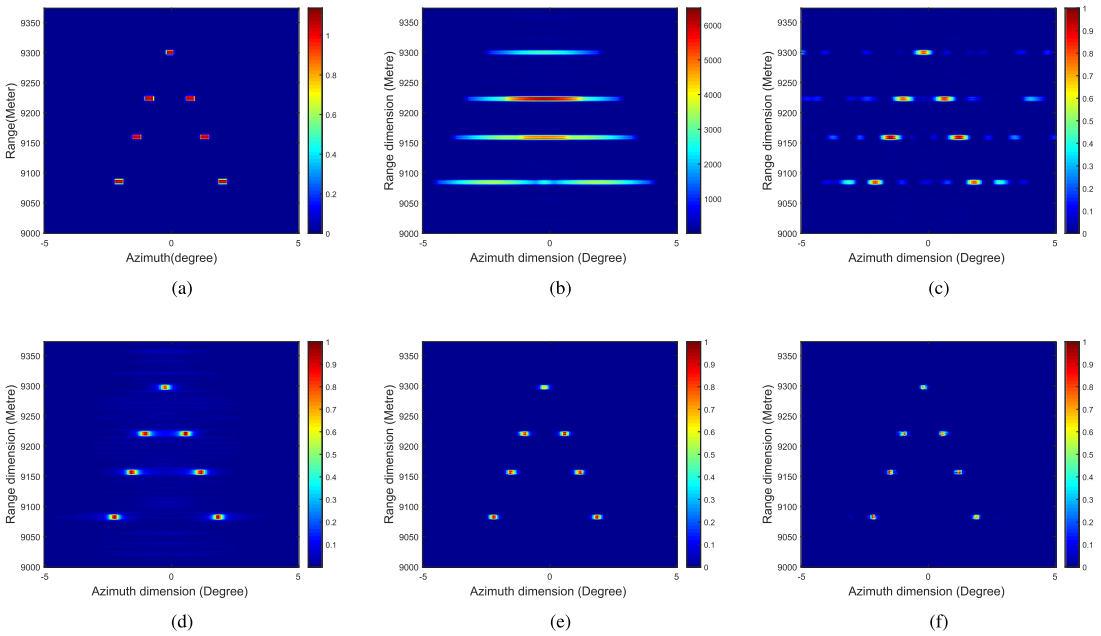

Fig. 9. 2-D area simulation result. (a) 2-D simulation scene. (b) Echo in SNR=25 dB. (c) TSVD method. (d) IAA method. (e) l_1-IRN method. (f) Proposed fast l_1-IRLSLS method.

TABLE VIII
ALGORITHM PARAMETERS AND CT OF 2-D SIMULATION

Algorithm	Parameters	CT
TSVD	$k = 17$	0.304746 s
IAA	$\lambda = 10$, $a = 1 \times 10^6$	15.913041 s
l_1-IRN	$\lambda = 10$, $\mu = 1000$	20.464822 s
fast l_1-IRLSLS	$\lambda = 10$, $q = 17$	2.042416 s

TABLE IX
SUPER-RESOLUTION PERFORMANCE COMPARISON OF 2-D SIMULATION

Algorithm	MSE	BSR
TSVD	0.2115	5.80
IAA	0.0829	9.67
l_1-IRN	1.5978e-04	11.19
fast l_1-IRLSLS	1.6754e-04	14.50

there are some shadows in the result. Fig. 9(e) and (f) is the result of the l_1-IRN method and the fast l_1-IRLSLS method, respectively. Intuitively, they have better imaging quality and are closer to the simulation scene. To quantitatively verify the super-resolution performance of the abovementioned methods, the profiles result of adjacent targets at distances of 9225 m is illustrated in Fig. 10. It is obvious that the fast l_1-IRLSLS method obtains narrower beam results, which can prove that it has a better super-resolution performance than other three methods. From Table IX, it is noted that the proposed fast l_1-IRLSLS method has the largest BSR and the second-lowest MSE value.

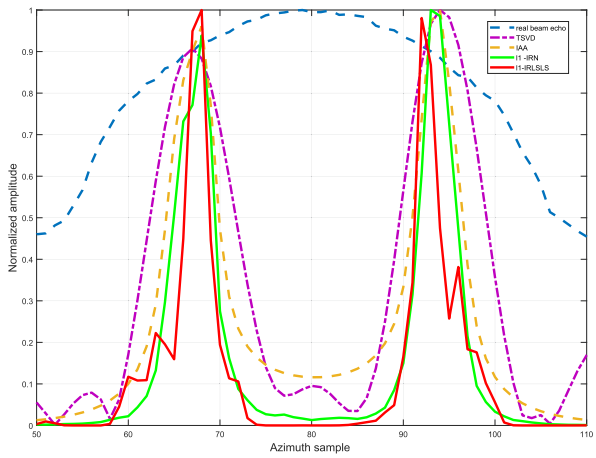

Fig. 10. Profiles result of adjacent targets at distances of 9225 m.

For the echo with dimensions of 598×167, the computational efficiency of the proposed algorithm is about 10 times of l_1-IRN, and 8 times of the IAA method seen from Table VIII.

C. Experimental Data

In Sections IV-A and IV-B, we have verified the proposed l_1-IRLSLS can achieve super-resolution imaging for 1-D point target and 2-D area scene, in this section, we will verify the performance of it on experimental data.

The experiment is undertaken at Ginkgo Avenue, University of Electronic Science and technology of China, Chengdu, China. The optical scene of Ginkgo Avenue is shown in the Fig 11(a), there are some ginkgo trees on both sides of the road. The experimental data are collected by an X-band radar. The X-band

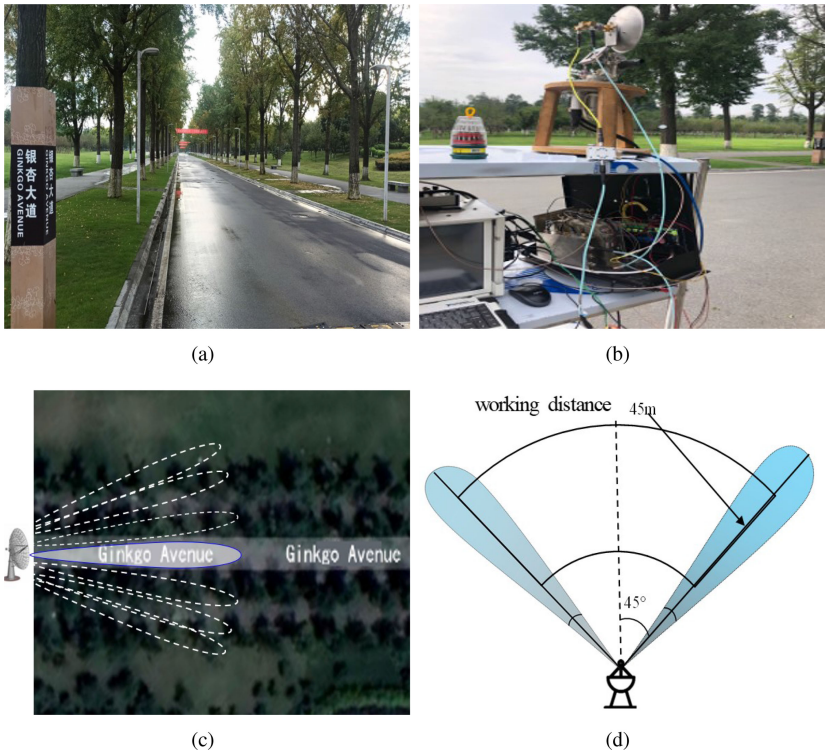

Fig. 11. Experiment taken on a stationary platform. (a) Experimental optical scene. (b) X-band radar. (c) Imaging geometry (side view). (d) Imaging geometry (vertical view).

TABLE X
ALGORITHM PARAMETERS AND CT OF EXPERIMENT

Algorithm	Parameters	CT
TSVD	$k = 30$	4.64577 s
IAA	$\lambda = 10$, $a = 1 \times 10^6$	51.824546 s
l_1-IRN	$\lambda = 10$, $\mu = 10000$	84.588174 s
fast l_1-IRLSLS	$\lambda = 10$, $q = 30$	12.123491 s

radar was fixed on a stationary platform shown in Fig 11(b). The radar sweeps the forward-looking region with the scanning speed of $72^\circ/\text{s}$ and at the PRF $= 200$ Hz from -45° to 45°. The antenna pattern for the radar system with the main-lobe width 5.1°, and working distance of radar is 45 m. The imaging mode is shown in Fig. 11(c) and (d).

Similarly, we give the parameters and CT of various algorithms in Table X. The range impulse compression is applied to the recorded data. The experimental result is shown in Fig. 12. Fig. 12(a) is the real beam result after impulse compression in range, many trees which are in the same range cell suffer low azimuth resolution and their echoes are overlapped. Fig. 12(b) is the result of TSVD. It only has limited resolution improvement, and many false sidelobe targets appear in the result. Fig. 12(c) is the result of IAA. The targets in the two red rectangles are distinguished, but they are not clear. In contrast, the l_1-IRN method and the fast l_1-IRLSLS method greatly improve azimuth resolution, and the targets in the two red rectangles are distinct. Visually, the l_1-IRN method and the fast l_1-IRLSLS method are almost same. It means that the super-resolution performance does not decrease by our fast l_1-IRLSLS method, but the CT has considerably decreased from 84.588 174 s to 12.123 491 s.

Also in order to intuitively reflect the super-resolution performance of the various algorithms, the profiles of the targets in the two red rectangles are listed in Figs. 13 and 14. From Figs. 13 and 14, we can see TSVD method and IAA both can sharpen real beam to a certain degree, but the l_1-IRN method and the fast l_1-IRLSLS method obtain narrower beam. Hence, the experimental data processing results also prove the effectiveness of the proposed method.

D. Comparison of Different Sparse Methods

In order to further verify the effectiveness of the fast sparse method in this article, the proposed fast IRLSLS method is compared with other sparse methods. Other sparse methods include MM method, SB algorithm, and IRN approach. The computational time (CT) of these methods with varying scanning scope from $-5^\circ - 5^\circ$ to $-160^\circ - 160^\circ$ will be investigated. Scanning speed is 30 $^\circ/\text{s}$, plus repetition frequency (PRF) is 2000 Hz. Correspondingly, the number of azimuth sampling points n varies from 667 to 4000. From Fig. 15, we can see that the CT of MM and IRN rises rapidly with the increase of azimuth sampling points, and the CT of SB grows relatively slowly. However, the CT of the proposed IRLSLS method has hardly grown, the CT savings provided by IRLSLS become more obvious with the increase of azimuth sampling points.

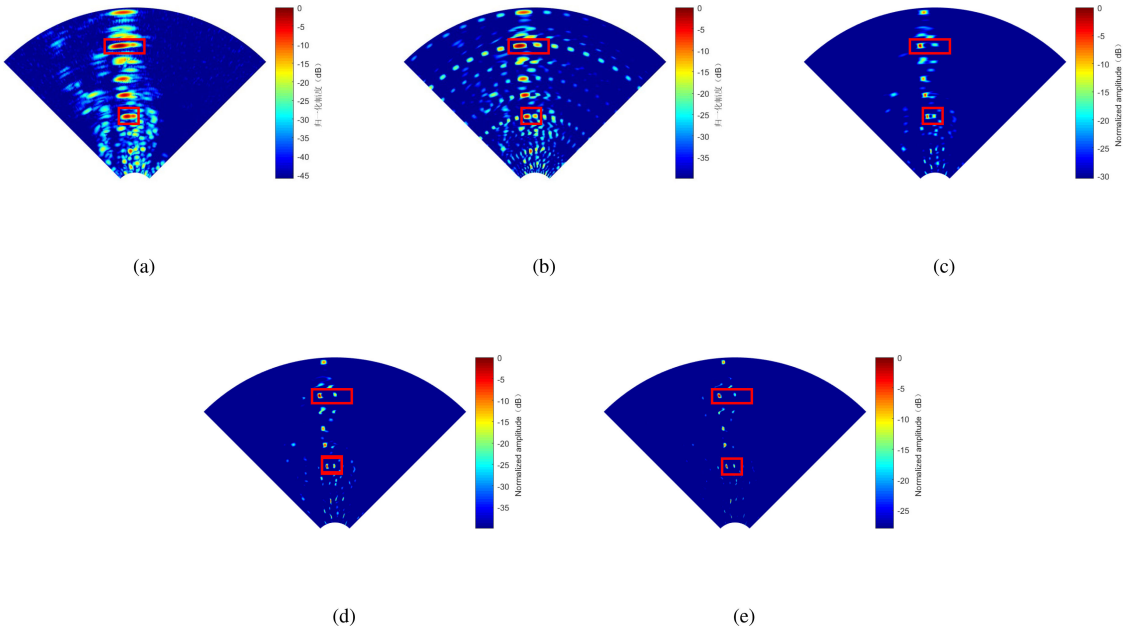

(a) (b) (c)

(d) (e)

Fig. 12. Experimental data result. (a) Real beam echo after impulse compression. (b) TSVD method. (c) IAA method. (d) l_1-IRN method. (e) Proposed fast l_1-IRLSLS method.

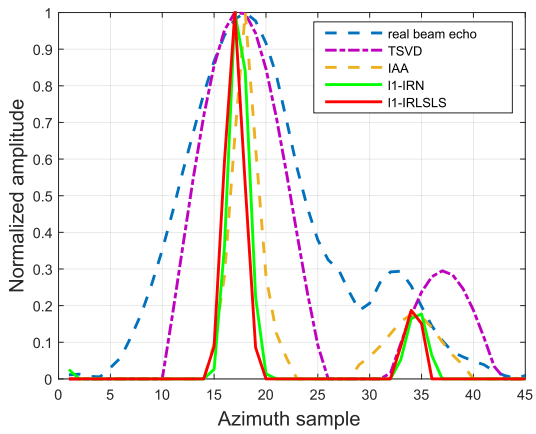

Fig. 13. Profiles of the targets in the above red rectangle.

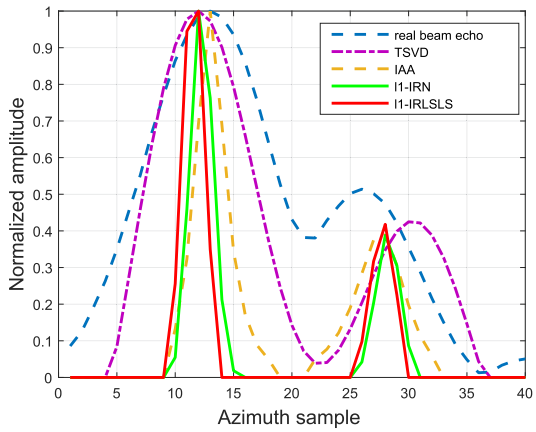

Fig. 14. Profiles of the targets in the below red rectangle.

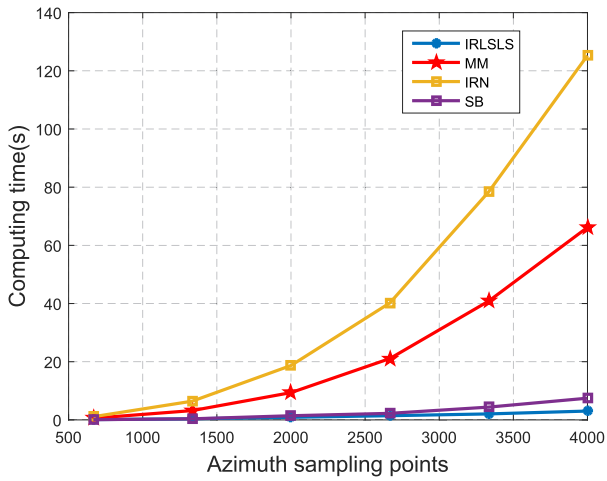

Fig. 15. Computation time of different sparse methods.

V. Conclusion

In this article, a fast sparse azimuth super-resolution method based on LS was proposed. Introducing the sparse constraint in the REGU framework, we transformed the super-resolution problem into an L_1 norm minimization problem. Exploiting the LS theory, this article constructed an embedded matrix. Then, echo matrix and antenna measurement matrix are compressed into much smaller matrices via multiplying them by this embedded matrix. Finally, the IRLS method is used to solve the reconstructed objective function, and the obtained solution is the result of super-resolution imaging. Much of the expensive computation can then be performed on the smaller matrices, thereby we reduced computational complexity.

In order to verify the effectiveness of the proposed algorithm, this article conducted 1-D point target simulation, 2-D area simulation, and experimental data. From the results of simulations and experimental data, the proposed method is almost the same in the super-resolution imaging performance as the l_1-IRN method, better than TSVD method and IAA method. However, compared with the l_1-IRN method, the proposed method effectively reduces the computational complexity and improves the real-time capability. In addition, this article also provides a comparison of the CT between the proposed fast sparse method and other sparse methods, which is shown in Fig. 15.

REFERENCES

[1] Q. Zhang, Y. Zhang, Y. Huang, and Y. Zhang, "Azimuth superresolution of forward-looking radar imaging which relies on linearized Bregman," *IEEE J. Sel. Topics Appl. Earth Observ. Remote Sens.*, vol. 12, no. 7, pp. 2032–2043, Jul. 2019.

[2] F. Soldovieri, G. Gennarelli, I. Catapano, D. Liao, and T. Dogaru, "Forward-looking radar imaging: A. comparison of two data processing strategies," *IEEE J. Sel. Topics Appl. Earth Observ. Remote Sens.*, vol. 10, no. 2, pp. 562–571, Feb. 2017.

[3] D. Liao and T. Dogaru, "Full-wave characterization of rough terrain surface scattering for forward-looking radar applications," *IEEE Trans. Antennas Propag.*, vol. 60, no. 8, pp. 3853–3866, Aug. 2012.

[4] Y. Zhang, X. Tuo, Y. Huang, and J. Yang, "A TV forward-looking super-resolution imaging method based on TSVD strategy for scanning radar," *IEEE Trans. Geosci. Remote Sens.*, vol. 58, no. 7, pp. 4517–4528, Jul. 2020.

[5] S. Uttam and N. A. Goodman, "Superresolution of coherent sources in real-beam data," *IEEE Trans. Aerosp. Electron. Syst.*, vol. 46, no. 3, pp. 1557–1566, Jul. 2010.

[6] Y. A. Pirogov *et al.*, "Superresolution and coherent phenomena in multi-sensor systems of millimeter-wave radio imaging," *Proc. SPIE*, vol. 5077, pp. 110–120, 2003.

[7] M. Fink and M. Tanter, "Multiwave imaging and super resolution," *Phys. Today*, vol. 63, no. 2, pp. 28–33, 2010.

[8] R. Bamler and P. Hartl, "Synthetic aperture radar interferometry," *Inverse Problems*, vol. 14, no. 4, pp. 25–32, 1998.

[9] F. Lenti, F. Nunziata, M. Migliaccio, and G. Rodriguez, "Two-dimensional TSVD to enhance the spatial resolution of radiometer data," *IEEE Trans. Geosci. Remote Sens.*, vol. 52, no. 5, pp. 2450–2458, May 2014.

[10] J. D. Shea, B. D. Van Veen, and S. C. Hagness, "A TSVD analysis of microwave inverse scattering for breast imaging," *IEEE Trans. Biomed. Eng.*, vol. 59, no. 4, pp. 936–945, Apr. 2012.

[11] X. Tuo, Y. Zhang, Y. Huang, and J. Yang, "Fast sparse-TSVD super-resolution method of real aperture radar forward-looking imaging," *IEEE Trans. Geosci. Remote Sens.*, to be published, doi: 10.1109/TGRS.2020.3027053.

[12] A. Gambardella and M. Migliaccio, "On the superresolution of microwave scanning radiometer measurements," *IEEE Geosci. Remote Sens. Lett.*, vol. 5, no. 4, pp. 796–800, Oct. 2008.

[13] T. Yardibi, J. Li, P. Stoica, M. Xue, and A. B. Baggeroer, "Source localization and sensing: A nonparametric iterative adaptive approach based on weighted least squares," *IEEE Trans. Aerosp. Electron. Syst.*, vol. 46, no. 1, pp. 425–443, Jan. 2010.

[14] G.-O. Glentis and A. Jakobsson, "Efficient implementation of iterative adaptive approach spectral estimation techniques," *IEEE Trans. Signal Process.*, vol. 59, no. 9, pp. 4154–4167, Sep. 2011.

[15] J. Karlsson, W. Rowe, L. Xu, G.-O. Glentis, and J. Li, "Fast missing-data IAA with application to notched spectrum SAR," *IEEE Trans. Aerosp. Electron. Syst.*, vol. 50, no. 2, pp. 959–971, Apr. 2014.

[16] Y. Zhang, D. Mao, Q. Zhang, Y. Zhang, Y. Huang, and J. Yang, "Airborne forward-looking radar super-resolution imaging using iterative adaptive approach," *IEEE J. Sel. Topics Appl. Earth Observ. Remote Sens.*, vol. 12, no. 7, pp. 2044–2054, Jul. 2019.

[17] J. Guan, J. Yang, Y. Huang, and W. Li, "Maximum a posteriori-based angular superresolution for scanning radar imaging," *IEEE Trans. Aerosp. Electron. Syst.*, vol. 50, no. 3, pp. 2389–2398, Jul. 2014.

[18] P. Zhang, Q. Chen, Z. Li, Z. Tang, J. Liu, and L. Zhao, "Superresolution SAR imaging algorithm based on MVM and weighted norm extrapolation," *ISPRS Int. Archives Photogrammetry, Remote Sens. Spatial Inf. Sci.*, vol. XL-7/W1, pp. 193–198, 2013.

[19] E. J. Candés and C. Fernandez-Granda, "Super-resolution from noisy data," *J. Fourier Anal. Appl.*, vol. 19, no. 6, pp. 1229–1254, 2013.

[20] H. Yasukawa, "Adaptive filtering for broad band signal reconstruction using spectrum extrapolation," in *Proc. IEEE Digit. Signal Process. Workshop Proc.*, 1996, pp. 169–172.

[21] F. Biondi, "Recovery of partially corrupted SAR images by super-resolution based on spectrum extrapolation," *IEEE Geosci. Remote Sens. Lett.*, vol. 14, no. 2, pp. 139–143, Feb. 2017.

[22] M. A. Herman and T. Strohmer, "High-resolution radar via compressed sensing," *IEEE Trans. Signal Process.*, vol. 57, no. 6, pp. 2275–2284, Jun. 2009.

[23] E. J. Candés and M. B. Wakin, "An introduction to compressive sampling," *IEEE Signal Process. Mag.*, vol. 25, no. 2, pp. 21–30, Mar. 2008.

[24] E. J. Candés, J. Romberg, and T. Tao, "Robust uncertainty principles: Exact signal reconstruction from highly incomplete frequency information," *IEEE Trans. Inf. Theory*, vol. 52, no. 2, pp. 489–509, Feb. 2006.

[25] E. J. Candes, J. K. Romberg, and T. Tao, "Stable signal recovery from incomplete and inaccurate measurements," *Commun. Pure Appl. Math.*, vol. 59, no. 8, pp. 1207–1223, 2006.

[26] L. C. Potter, E. Ertin, J. T. Parker, and M. Cetin, "Sparsity and compressed sensing in radar imaging," *Proc. IEEE*, vol. 98, no. 6, pp. 1006–1020, Jun. 2010.

[27] Q. Zhang, Y. Zhang, Y. Huang, and Y. Zhang, "Azimuth superresolution of forward-looking radar imaging which relies on linearized bregman," *IEEE J. Sel. Top. Appl. Earth Observ. Remote Sens.*, vol. 12, no. 7, pp. 2032–2043, Jul. 2019.

[28] J. Matamoros, S. M. Fosson, E. Magli, and C. Antón-Haro, "Distributed ADMM for in-network reconstruction of sparse signals with innovations," *IEEE Trans. Signal Inf. Process. Netw.*, vol. 1, no. 4, pp. 225–234, Dec. 2015.

[29] B. Wohlberg, "Efficient algorithms for convolutional sparse representations," *IEEE Trans. Image Process.*, vol. 25, no. 1, pp. 301–315, Jan. 2016.

[30] Y. Sun, P. Babu, and D. P. Palomar, "Majorization-minimization algorithms in signal processing, communications, and machine learning," *IEEE Trans. Signal Process.*, vol. 65, no. 3, pp. 794–816, Feb. 2017.

[31] B. K. Sriperumbudur, D. A. Torres, and G. R. Lanckriet, "A majorization-minimization approach to the sparse generalized eigenvalue problem," *Mach. Learn.*, vol. 85, no. 1/2, pp. 3–39, 2011.

[32] Y. Zhang, Z. Dong, P. Phillips, S. Wang, G. Ji, and J. Yang, "Exponential wavelet iterative shrinkage thresholding algorithm for compressed sensing magnetic resonance imaging," *Inf. Sci.*, vol. 322, pp. 115–132, 2015.

[33] K. Xiong, G. Zhao, G. Shi, and Y. Wang, "A convex optimization algorithm for compressed sensing in a complex domain: The complex-valued split Bregman method," *Sensors*, vol. 19, no. 20, pp. 4540–4562, 2019.

[34] J. Wang, J. Ma, B. Han, and Q. Li, "Split Bregman iterative algorithm for sparse reconstruction of electrical impedance tomography," *Signal Process.*, vol. 92, no. 12, pp. 2952–2961, 2012.

[35] R. Chartrand and W. Yin, "Iteratively reweighted algorithms for compressive sensing," in *Proc. IEEE Int. Conf. Acoust., Speech Signal Process.*, 2008, pp. 3869–3872.

[36] Q. Zhang, Y. Zhang, Y. Huang, Y. Zhang, W. Li, and J. Yang, "Sparse with fast mm superresolution algorithm for radar forward-looking imaging," *IEEE Access*, vol. 7, pp. 105 247–105257, 2019.

[37] A. Beck and M. Teboulle, "A fast iterative shrinkage-thresholding algorithm for linear inverse problems," *SIAM J. Imag. Sci.*, vol. 2, no. 1, pp. 183–202, 2009.

[38] A. Chambolle and C. Dossal, "On the convergence of the iterates of the fast iterative shrinkage/thresholding algorithm," *J. Optim. Theory Appl.*, vol. 166, no. 3, pp. 968–982, 2015.

[39] Y. Zhang, Y. Zhang, W. Li, Y. Huang, and J. Yang, "Super-resolution surface mapping for scanning radar: Inverse filtering based on the fast iterative adaptive approach," *IEEE Trans. Geosci. Remote Sens.*, vol. 56, no. 1, pp. 127–144, Jan. 2018.

[40] Y. Zhang, W. Li, Y. Zhang, Y. Huang, and J. Yang, "A fast iterative adaptive approach for scanning radar angular superresolution," *IEEE J. Sel. Top. Appl. Earth Observ. Remote Sens.*, vol. 8, no. 11, pp. 5336–5345, Nov. 2015.

[41] D. P. Woodruff *et al.*, "Sketching as a tool for numerical linear algebra," *Found. Trends Theor. Comput. Sci.*, vol. 10, no. 1/2, pp. 1–157, 2014.

[42] F. Gama, A. G. Marques, G. Mateos, and A. Ribeiro, "Rethinking sketching as sampling: Linear transforms of graph signals," in *Proc. 50th Asilomar Conf. Signals, Syst. Comput.*, 2016, pp. 522–526.
[43] Z. Song, R. Wang, L. Yang, H. Zhang, and P. Zhong, "Efficient symmetric norm regression via linear sketching," in *Proc. Adv. Neural Inf. Process. Syst.*, 2019, pp. 828–838.
[44] P. Indyk, Sketching, Streaming and Sublinear-Space Algorithms, *MIT*, Cambridge, MA, USA, 2007.
[45] N. Halko, P.-G. Martinsson, and J. A. Tropp, "Finding structure with randomness: Probabilistic algorithms for constructing approximate matrix decompositions," *SIAM Rev.*, vol. 53, no. 2, pp. 217–288, 2011.
[46] L. Mirsky, "Symmetric gauge functions and unitarily invariant norms," *Quart. J. Math.*, vol. 11, no. 1, pp. 50–59, 1960.
[47] G. H. Golub, M. Heath, and G. Wahba, "Generalized cross-validation as a method for choosing a good ridge parameter," *Technometrics*, vol. 21, no. 2, pp. 215–223, 1979.
[48] N. Halko, P.-G. Martinsson, and J. A. Tropp, "Finding structure with randomness: Stochastic algorithms for constructing approximate matrix decompositions," to be published.
[49] L. Chen, "Finding structure with randomness: Probabilistic algorithms for constructing approximate matrix decompositions," to be published.
[50] T. Wu, S. A. N. Sarmadi, V. Venkatasubramanian, A. Pothen, and A. Kalyanaraman, "Fast SVD computations for synchrophasor algorithms," *IEEE Trans. Power Syst.*, vol. 31, no. 2, pp. 1651–1652, Mar. 2016.
[51] N. B. Erichson, S. Voronin, S. L. Brunton, and J. N. Kutz, "Randomized matrix decompositions using R," 2016, *arXiv:1608.02148*.
[52] P. C. Hansen and D. P. OLeary, "The use of the l-curve in the regularization of discrete ill-posed problems," *SIAM J. Sci. Comput.*, vol. 14, no. 6, pp. 1487–1503, 1993.

Xingyu Tuo (Student Member, IEEE) received the B.S. degree in photoelectric information science and engineering from the Chongqing University, Chongqing, China, in 2018. He is currently working toward the Ph.D. degree in information and communication engineering with the University of Electronic Science and Technology of China, Chengdu, China.

His research interests include radar signal processing and sparse signal processing.

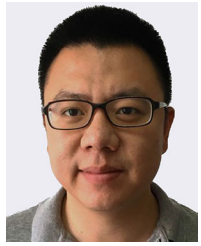

Yin Zhang (Member, IEEE) received the B.S. and Ph.D. degrees in electronic information engineering from the University of Electronic Science and Technology of China (UESTC), Chengdu, China, in 2008 and 2016, respectively.

From 2015 to 2016, he was a Visiting Student with the University of Delaware, Newark, DE, USA. He is currently an Associate Research Fellow with the School of Information and Communication Engineering, UESTC. His research interests include radar imaging and signal processing in related radar applications.

Yulin Huang (Senior Member, IEEE) received the B.S. and Ph.D. degrees in electronic information engineering from the School of Electronic Engineering, University of Electronic Science and Technology of China (UESTC), Chengdu, China, in 2002 and 2008, respectively.

From 2013 to 2014, he was a Visiting Researcher with the University of Houston, Houston, TX, USA. He is currently an Professor with the School of Information and Communication Engineering, UESTC. His research interests include synthetic aperture radar, target detection and recognition, artificial intelligence, and machine learning.

Jianyu Yang (Member, IEEE) received the B.S. degree from the National University of Defense Technology, Changsha, China, in 1984, and the M.S. and Ph.D. degrees from the University of Electronic Science and Technology of China (UESTC), Chengdu, China, in 1987 and 1991, respectively.

He is currently a Professor with UESTC. His research interests include synthetic aperture radar and statistical signal processing.

Dr. Yang is currently a Senior Editor for the *Chinese Journal of Radio Science* and the *Journal of Systems Engineering and Electronics*.